

ORIGINAL ARTICLE

Journal Section

Characterization of Strain Parameters in a Diamond Nanophotonic Structure

Ayan Majumder^{1*} | Vivek K Shukla^{3*} | Anuj Bathla^{2,1}
 | Brajesh S. Yadav⁴ | Nanhey Singh⁴ | Padmnabh
 Rai^{3†} | Kasturi Saha^{1‡}

¹Department of Electrical Engineering,
 Indian Institute of Technology Bombay,
 Powai, Mumbai-400076, India

²Center for Research in Nano Technology
 and Science, Indian Institute of Technology
 Bombay, Powai, Mumbai-400076, India

³School of Physical Sciences, UM-DAE
 Centre for Excellence in Basic Sciences,
 University of Mumbai, Mumbai-400098,
 India

⁴Solid State Physics Laboratory, Lucknow
 Road, Timarpur, Delhi-110054, India

Correspondence

Department of Electrical Engineering,
 Indian Institute of Technology Bombay,
 Powai, Mumbai-400076, India
 Email: kasturis@ee.iitb.ac.in,
 194076009@iitb.ac.in

Present address

†

Funding information

Negatively charged nitrogen-vacancy (NV^-) centers and other color centers in diamonds have emerged as promising platforms for quantum communication, quantum information processing, and nanoscale sensing, owing to their long spin coherence times, fast spin control, and efficient photon coupling. Deterministic placement of individual color centers into nanophotonic structures is critical for scalable device integration, and ion implantation is the most viable technique. Nanofabrication processes, including diamond etching, are essential to realize these structures but can introduce crystal strain through lattice damage. In this work, we investigate the impact of ion implantation and nanofabrication-induced strain on the electronic spin levels of NV^- centers. We demonstrate that the zero-field continuous-wave optically detected magnetic resonance (CW-ODMR) spectrum serves as a sensitive probe of local crystal strain, providing both quantitative and directional information. Furthermore, we present a model that explains the strain-induced features observed in the ODMR spectra of the single NV^-

Abbreviations:

* Equally contributing authors.

center, offering a framework to characterize the strain effects in diamond-based nanophotonic devices.

KEY WORDS

Nitrogen-vacancy center, nanophotonics, crystal-strain, ion-implantation

1 | INTRODUCTION

Color defect centers in diamond are promising candidates for quantum communication [1], quantum information processing [2, 3], and nanoscale sensing [4, 5] applications due to their long coherence times, fast spin-state manipulation, and the ability to be optically initialized and read out [6]. Among these, the negatively charged nitrogen-vacancy (NV^-) center is particularly notable, as it can be optically initialized and read out even at room temperature [6]. The electronic spin states of NV^- centers are highly sensitive to variations in electric and magnetic fields, temperature, and local strain in the host diamond lattice [7]. Owing to this sensitivity, single NV^- centers can be incorporated into diamond nanopillars or nanodiamonds, serving as atomic-scale probes for super-resolution scanning probe microscopy [8] or targeted *in vivo* magnetic noise sensing [9] in a cell environment [10]. Additionally, thin layers (a few nanometers thick) of high-density NV^- centers can be used for magnetic imaging of samples, offering a wide field of view, micrometer-scale resolution [7, 11], and high magnetic field sensitivity [12].

For all such applications, improving light-matter interaction [13, 14, 15, 16] and efficient fluorescence collection [17] is essential to enhance the fidelity of quantum operations [1, 18]. In particular, improving the fidelity of quantum state transfer from photonic qubits to spin qubits requires enhanced light-matter interaction, which can be achieved by placing the NV^- center in a high-cooperativity optical cavity [15]. Ion implantation is a promising technique for positioning single emitters at desired locations within nanophotonic cavities [1, 15, 19]. Similarly, advanced nanofabrication techniques are crucial for the development of photonic structures that enhance both light-matter interaction and photon collection efficiency [20, 21].

However, both ion implantation and nanofabrication introduce lattice damage that results in crystal strain within the diamond substrate [22, 23, 24]. Several methods exist for strain characterization, including those based on SiV^- centers [25, 26], NV^- center zero-phonon line shifts [22, 27]. A widely used technique is zero-field optically detected magnetic resonance (ODMR) [27]. Previous studies have used ODMR to measure axial and non-axial strain components using preferentially aligned NV^- centers in unprocessed polycrystalline diamond and nanocrystals containing few NV^- centers, or by analyzing the splitting of single- NV^- ODMR signals [28, 29]. Zero-field ODMR spectroscopy has also been utilized to probe strain components in diamond waveguides, as shown by M. Sahnawaz Alam et al. [23]. In this work, diamond waveguides were fabricated using femtosecond laser writing, where focused laser pulses induced structural changes—such as amorphization and graphitization—that generated strain within the crystal lattice. In our study, we report an asymmetric splitting in the zero-field ODMR spectra of both nitrogen ion-implanted bulk diamond and diamond nanopillar samples. To understand the origin of this asymmetry, we present a theoretical model that links the observed spectral features to strain-induced modifications in the spin Hamiltonian of individual NV^- centers.

This paper is organized as follows. In Subsec. 2.1, we describe the SRIM (Stopping and Range of Ions in Matter) simulations and the sample preparation process for ion-implanted single-crystal diamond, including Three-Dimensional Finite-Difference Time-Domain (3D-FDTD) simulations used to optimize the nanopillar dimensions and details of the

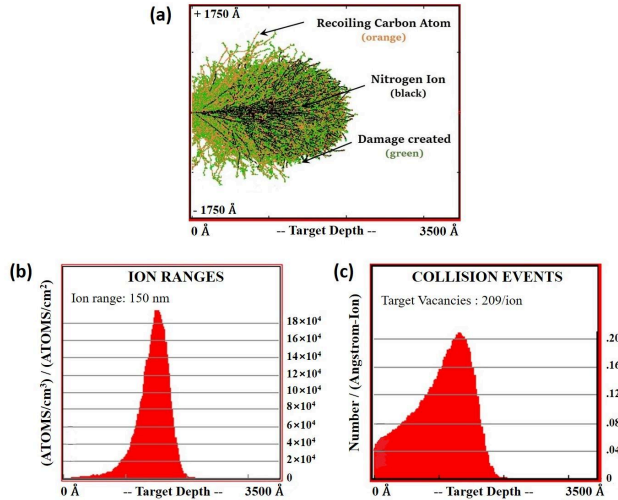


FIGURE 1 Results of the SRIM simulation of nitrogen-implanted diamond conducted at energy 130 keV. (a) Ion trajectories of nitrogen ions, recoiled carbon atoms, and created vacancies are depicted with different colors, (b) ion distribution profile, and (c) target carbon vacancies, as a function of depth.

fabrication process. Subsec. 2.2 presents Raman spectroscopy measurements used to characterize strain in the diamond crystal. In Subsec. 2.3, we describe the measurement of magnetic resonance spectra for NV^- centers in both bulk diamond and nanophotonic structures. Subsec. 2.4 introduces a theoretical model explaining the origin of asymmetric splitting in zero-field ODMR spectra from the perspective of a single NV^- center. We conclude in Sec. 3, and Sec. 4 provides details of our experimental setups for Raman spectroscopy and the microwave-integrated laser scanning confocal microscopy system.

2 | RESULTS AND DISCUSSION

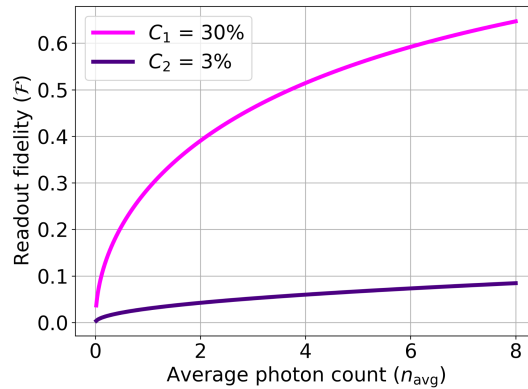
2.1 | Sample Preparation

2.1.1 | SRIM Simulation and Nitrogen-ion Implantation

The single-crystal diamond (SCD) samples were grown on (100)-oriented (Type IIa) diamond substrates ($7.5 \text{ mm} \times 7.2 \text{ mm} \times 0.8 \text{ mm}$, in-house CVD-grown SCD with nitrogen concentration $< 100 \text{ ppb}$) using a custom-built microwave plasma CVD reactor (2.45 GHz, 6 kW). The optimal growth conditions for homoepitaxial SCDs are as follows: Microwave power 5000 W, CH_4/H_2 flow ratio 10%, N_2/H_2 flow ratio 0.004%, substrate temperature 950°C, and chamber pressure 125 Torr. After growth, the samples underwent laser cutting, mechanical polishing, and cleaning using a boiling ternary acid mixture ($\text{HNO}_3 : \text{HClO}_4 : \text{H}_2\text{SO}_4 = 1 : 1 : 1$ by volume) to selectively etch away graphitic carbon from the diamond surface. The CVD-grown diamond samples (labeled DRM-8, 9, and 10) were then employed for nitrogen ion implantation. The sample dimensions were $5.0 \text{ mm} \times 5.4 \text{ mm} \times 0.4 \text{ mm}$, $4.8 \text{ mm} \times 5.1 \text{ mm} \times 0.4 \text{ mm}$, and $6.0 \text{ mm} \times 5.0 \text{ mm} \times 0.3 \text{ mm}$ for DRM-8, DRM-9, and DRM-10, respectively. Ion implantation was carried out using nitrogen ions ($^{14}\text{N}^+$, energy 130 keV) at room temperature with three different doses: 1×10^{13} (DRM-8), 1×10^{14}

TABLE 1 SRIM simulation results for vacancy concentration at different ion fluences in the diamond matrix.

Sample name	Implantation Energy (keV)	Ion Fluence/Dose (ions/cm ²)	Damage (vacancies/cm ³)
DRM-8	130	1×10^{13}	2.08×10^{20}
DRM-9	130	1×10^{14}	2.09×10^{21}
DRM-10	130	1×10^{16}	2.15×10^{23}

**FIGURE 2** Simulated readout fidelity as a function of n_{avg} for both a single NV[−] center and an ensemble of NV[−] centers. C_1 and C_2 represent the fluorescence contrast for the single NV[−] center and the ensemble, respectively. The readout duration for this simulation is 300 ns.

(DRM-9), and 2×10^{16} (DRM-10) ions/cm², respectively, utilizing IBS, IMC200 ion implanter. A homogeneous circular ion beam of diameter 1 mm was rastered over the sample to achieve uniform irradiation at the desired dose. The samples were subsequently annealed at 1000°C in an argon (Ar) atmosphere for 2 h at a chamber pressure of 5×10^{-3} mbar to restore the implantation-induced lattice damages. Additionally, the samples were thoroughly acid-cleaned to eliminate any carbon or graphitic deposits from the surface before conducting any measurements.

Monte-Carlo simulations were performed using the stopping and range of ions in matter (SRIM) software (version 2008.04) to estimate the concentration of implantation-induced vacancies in the diamond matrix [30]. The estimated trajectory of nitrogen ions and recoiled carbon atoms resulting from collisions in the diamond matrix is depicted in Fig. 1(a). A nearly Gaussian distribution of nitrogen ions in the diamond matrix shows a peak concentration at a depth of 150 nm below the top surface (Fig. 1(b)). The vacancy density, signifying the extent of lattice damage caused by the displacement of carbon atoms from their lattice sites, is shown in Fig. 1(c). Table 1 summarizes the implantation energy, dose, and corresponding estimated damage (vacancies/cm³) for the nitrogen-implanted diamond samples.

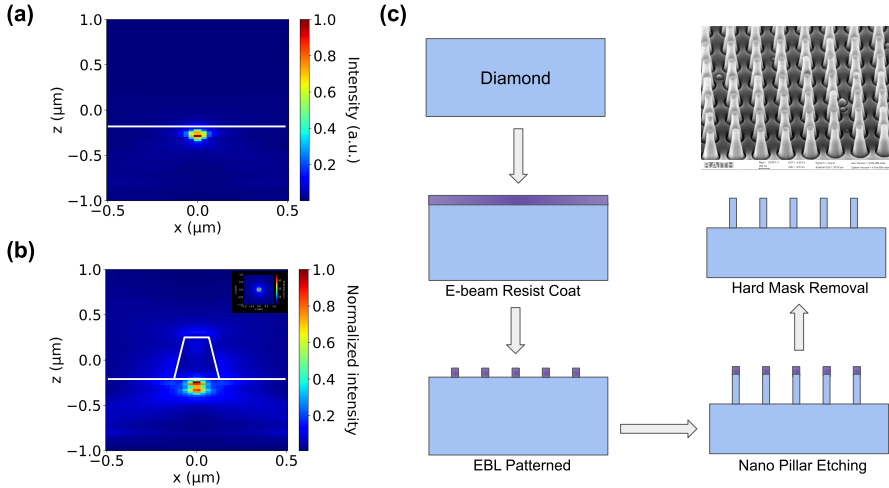


FIGURE 3 (a) Simulated normalized intensity distribution of a dipole emitter inside a diamond slab. (b) Simulated normalized intensity distribution of a dipole emitter with a diamond nanopillar. The inset figure shows the intensity distribution in the XY plane, which is around 600 nm above the dipole emitter. (c) Schematic of the fabrication process flow of the diamond nanopillar sample. The SEM image of the fabricated diamond nanopillar sample is shown here.

2.1.2 | FDTD-Simulation and Fabrication of Diamond Nanopillar

Improving the photon collection efficiency is essential for quantum sensing [21] and quantum network [1] applications. The readout fidelity determines the sensitivity as well as the spin-spin entanglement generation rate based on single-photon detection. The n_{avg} and the contrast (C) determine the readout fidelity (\mathcal{F}) [12],

$$\mathcal{F} = \frac{C \sqrt{n_{avg}}}{\sqrt{C^2 n_{avg} + 1}} \quad (1)$$

The average number of photons collected per NV^- center per measurement is denoted by n_{avg} . Improving the readout fidelity necessitates increasing n_{avg} , which is directly enhanced by the photon collection efficiency. Figure 2 shows the simulated readout fidelity as a function of n_{avg} for both a single NV^- center and an ensemble of NV^- centers. The high refractive index of diamond (approximately 2.41) causes total internal reflection confinement, preventing photons from being efficiently collected. The calculated collection efficiencies for photons emitted directly through the $\{100\}$ diamond surface are 3.7% and 10.4% for air and oil-immersion objectives, respectively, with numerical apertures of 0.95 and 1.49 [12]. Modifying the diamond surface is helpful in increasing photon collection efficiency. Three-dimensional finite-difference time-domain (3D-FDTD) simulations were performed to determine the dimensions for the diamond nanopillars to enhance light collection [20, 21]. Two cases are simulated, in the first case, all possible dipole orientations based on the four possible NV -center orientations [31] with center wavelength 637 nm are inside the diamond crystal, which is around 10 nm below the crystal surface. In the second case, a truncated conical-shaped diamond nanopillar is added to the crystal surface. The refractive index of the diamond was 2.418 in both situations

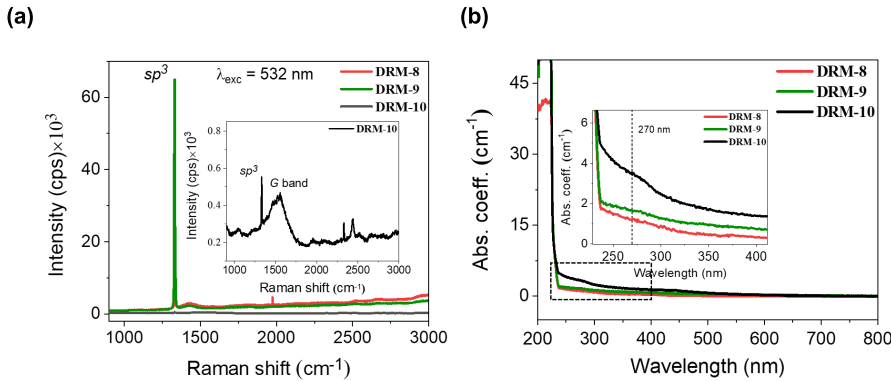


FIGURE 4 (a) Raman and corresponding (b) post-annealing UV-visible absorption spectra of the diamond samples. The spectra shown in the insets are their enlarged views.

[14]. The pillar height was 576 nm, and its top and bottom surfaces had diameters of approximately 146 nm and 304 nm, respectively. A perfectly matched layer (PML) was considered around the simulation zone to prevent reflection from the simulation boundaries. Figures 3(a) and (b) show the simulated normalized intensity distributions at 637 nm wavelength. The inset figure shows the intensity distributions collected by the intensity-measurement monitor. The simulation results show an enhancement and confinement in PL when the dipole emitter is considered close to the diamond nanopillar. Compared with the pristine diamond crystal sample, the light emitted by the diamond nanopillar sample was more directed and focused.

The diamond pillar fabrication was carried out based on the simulated parameters. Figure 3(c) presents a flowchart of the fabrication process. Initially, the diamond substrate was cleaned using a tri-acid solution. A bilayer resist (495KA4 and 950KA2 PMMA) was then spin-coated onto the substrate and baked at 180°C. Electron beam lithography (Raith-150Two) was used for patterning. Subsequently, a 60 nm thick titanium (Ti) layer was deposited using a sputtering technique. The diamond etching was performed using inductively coupled plasma reactive ion etching (ICP-RIE), following the defined pattern. Finally, hydrofluoric acid (HF) was used to remove the residual Ti mask. The scanning electron microscopy (SEM) image of the fabricated diamond nanopillar array is shown in Figure 3(c).

2.2 | Raman Spectroscopy

Raman measurements were performed to determine the distribution and evolution of the diamond Raman peak position and the defect peaks that arise from sample irradiation. The Raman signature of the implanted samples is evident by the narrow one-phonon peak that appeared at 1332 cm^{-1} , with no significant background observed [32]. Upon implantation, the one-phonon peak broadens and shifts to higher wave numbers, indicating damage to the diamond lattice. The damage caused by ion implantation, at 1×10^{13} and 1×10^{14} ions/ cm^2 fluences, remains below the critical graphitization threshold (2×10^{22} vacancies/ cm^3), which allows the sp^3 -bonding to be preserved in the samples

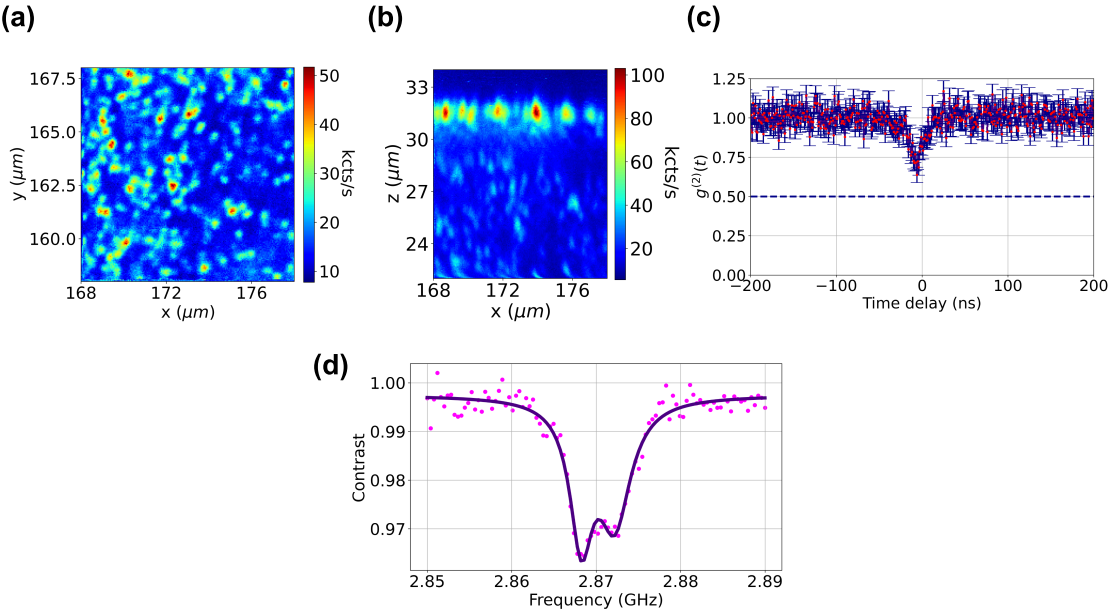


FIGURE 5 (a) XY confocal scan of the nitrogen-ion-implanted sample. (b) XZ confocal scanning of the nitrogen-ion-implanted sample. (c) Second-order correlation measurement data at a diffraction-limited spot. (d) Zero-field ODMR spectrum at the same diffraction-limited spot. Two Lorentzian profiles were used to fit the experimental data. There was an imbalance between the two Lorentzian peaks in the zero-field CW-ODMR data.

DRM-8 and DRM-9 after annealing [32, 33]. High fluences (1×10^{16} ions/cm 2) cause significant lattice damage in the diamond sample (DRM-10), as evidenced by the weakened diamond Raman peak intensity (Fig. 4(a), inset). Since the intensity of the diamond peak correlates with the volume of regular diamond within the laser spot, its reduction can serve as an estimate of the degree of amorphization [33]. Annealing leads to a slight reduction in the damaged region but does not significantly enhance the intensity of the diamond Raman peak, instead resulting in a graphite-related G peak at 1580 cm $^{-1}$. Figure 4(b) presents the room temperature UV-visible absorption spectra (200 – 800 nm) of ion-implanted diamond samples. The DRM-10 sample shows notably stronger absorption at 270 nm (Fig. 4(b), inset), which correlates with its higher substitutional nitrogen (N_s^0) concentration. The N_s^0 concentration was determined by fitting the UV absorption spectrum (300-450 nm region) with a second-order polynomial [34, 35], using $[N_s^0]$ (ppm) = $0.56 \times \alpha_{270}$, where α_{270} (cm $^{-1}$) is the absorption coefficient at 270 nm. The estimated nitrogen concentrations were 300 ppb (DRM-8), 250 ppb (DRM-9), and 760 ppb (DRM-10).

2.3 | Magnetic Resonance Spectroscopy of NV-Centers in Bulk Diamond Crystal and Nanophotonic Structure

A home-built laser-scanning confocal microscope with a microwave excitation module was used for confocal imaging of the bulk diamond sample and spectroscopy of the color centers in the diamond. Figures 5(a), (b), and 6(a) show

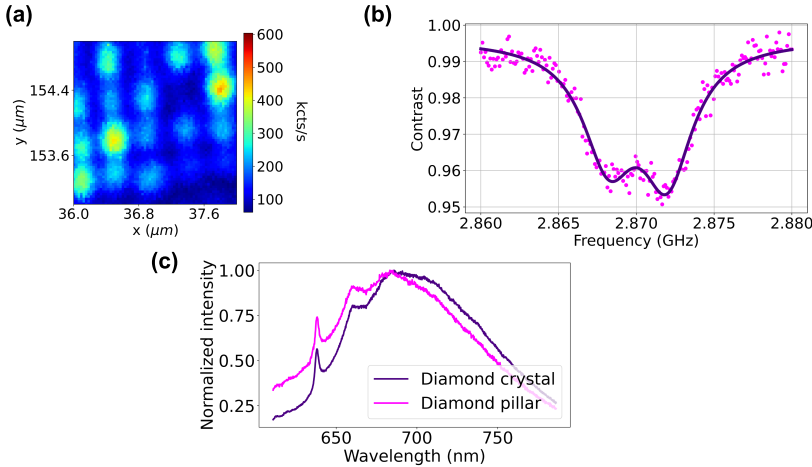


FIGURE 6 (a) Confocal image of the diamond nanopillar array. (b) Zero-field ODMR spectrum of diamond nanopillar. Two Lorentzian profiles are considered to fit the experimental data. There is an imbalance between the two Lorentzian peaks in the zero-field CW-ODMR data. (c) Photoluminescence excitation spectroscopy data for the pristine and diamond nanopillar samples.

confocal images of the samples. The bright spots are clusters of NV^- centers in the diffraction-limited spot. In Figure 6(a), the photon counts from the diamond nanopillars are five times higher than the background counts. The PL enhancement was consistent with the simulated scenario. Figure 6(c) shows the photoluminescence excitation (PLE) spectroscopy [36] data. Figure 5(c) shows the second-order correlation measurement, which confirms the number of emitters at the diffraction-limited spot. For both samples, the number of NV^- centers at the diffraction-limited spot was approximately 3–4. The ground state of the NV^- center is a spin triplet (3A_2), with its sublevels experiencing energy splitting due to spin–spin interactions, resulting in spin states with spin projection $|m_s = 0\rangle$ and $|m_s = \pm 1\rangle$, separated by $D = 2.87$ GHz when no external magnetic field is applied [8, 37]. In this context, m_s refers to the spin projection along the intrinsic quantization axis of the NV^- center, which corresponds to the direction towards the nitrogen atom and vacancy. The defect center can be optically excited via a spin-conserving transition to the excited level 3E , which is also a spin triplet. In addition, the 3E excited state has an orbital doublet configuration that is effectively averaged at room temperature, resulting in a zero-field splitting of $D = 1.42$ GHz, maintaining the same quantization axis and gyromagnetic ratio as in the ground state [8, 37, 38]. After being optically excited to the 3E level, the NV^- center can relax back either by emitting photons through a radiative transition, which produces broad red (600 – 800 nm) photoluminescence (PL), or via a secondary pathway involving nonradiative intersystem crossing (ISC) to singlet states [2, 8]. Experimental observations indicated the existence of two singlet states located between the ground and excited states of the NV^- center, which are significant in the spin dynamics of the NV^- center. Specifically, while optical transitions predominantly conserve spin ($\Delta m_s = 0$), non-radiative ISCs to the 1E singlet state exhibit strong spin selectivity because the ISC transition rate from the $|m_s = 0\rangle$ sublevel is much lower than that from $|m_s = \pm 1\rangle$ [2, 8]. In contrast, the NV^- center favors the decay from the lowest 1A_1 singlet state to the ground state $|m_s = 0\rangle$. These spin-selective mechanisms result in significant electron spin polarization towards the $|m_s = 0\rangle$ state,

achieved through optical pumping. Moreover, because ISCs are nonradiative processes, the intensity of the NV⁻ center PL is considerably enhanced when the $|m_s = 0\rangle$ state is populated [2, 8]. This spin-dependent response in PL allows the detection of electron spin resonance (ESR) or optically detected magnetic resonance (ODMR) at the level of individual defects through an optical readout [2, 8]. When a single NV⁻ defect that was initially prepared in the $|m_s = 0\rangle$ state via optical pumping was subjected to a resonant microwave field, resulting in a transition to the $|m_s = \pm 1\rangle$ spin state, a decrease in the PL signal was detected. The simplest ground-state Hamiltonian of the NV⁻ center is,

$$H = hDS_z^2 + hE(S_x^2 - S_y^2) + g\mu_B\vec{B} \cdot \vec{S}$$

$$\Rightarrow H = hDS_z^2 + g\mu_B B_{NV} S_z + g\mu_B(B_x S_x + B_y S_y) + hE(S_x^2 - S_y^2) \quad (2)$$

where h is the Planck's constant, D is the zero-field splitting factor, g is the Landé g-factor of the NV⁻ center electronic spin, μ_B is the Bohr magneton, and B_{NV} is the magnetic field along the NV center quantization axis [2, 8]. The off-axis zero-field splitting parameter E results from local strain in the host diamond matrix. In the weak magnetic field amplitudes, the eigen-energy of the ground state Hamiltonian or the ESR frequencies of the NV⁻ center,

$$\nu_{\pm}(B_{NV}) = D \pm \sqrt{\left(\frac{g\mu_B}{h} B_{NV}\right)^2 + E^2}. \quad (3)$$

At a zero bias field ($B_{NV} = 0$), the ESR frequencies are $\nu_{\pm} = D \pm E$ [2, 8]. In most cases, symmetric splitting of the zero-field ODMR spectrum in a bulk crystal sample has been reported [8, 24]. Here, asymmetric splitting of the zero-field ODMR peak [23] for both the nitrogen-ion-implanted and diamond nanopillar samples was observed. It is well known that ion implantation damages the lattice structure of diamond crystals, and a high-temperature annealing process is generally used to generate NV⁻ centers, which also repair lattice damage to a certain extent [39, 40, 41]. Similarly, in nano-fabrication processes, the ICP-RIE process is used to etch the diamond crystal, which also damages the diamond lattice. Owing to the deformation of the lattice structure, asymmetric splitting in the zero-field ODMR spectrum was observed, as shown in Figures 5(d) and 6(b) [23]. In Section 2.4, a mathematical model is presented to explain the imbalance between the two Lorentzian peaks of the zero-field ODMR data for both samples.

2.4 | Strain Modeling

In this section, a model is presented to explain asymmetric splitting in the zero-field ODMR spectrum based on a single NV⁻ center in a diamond crystal. The Hamiltonian for the orbital ground state of an NV⁻ center in the absence of a static magnetic field and the presence of strain and microwave driving field can be described as [12, 23, 24],

$$H = hDS_z^2 + \lambda(t)\vec{B}_{mw} \cdot \vec{S} + H_{strain} \quad (4)$$

$$\frac{H_{strain}}{h} = M_z S_z^2 + M_x(S_y^2 - S_x^2) + M_y(S_x S_y + S_y S_x) + N_x(S_x S_z + S_z S_x) + N_y(S_y S_z + S_z S_y) \quad (5)$$

where h is Planck's constant, $D = 2.87$ GHz is the zero-field splitting parameter, $\lambda(t)\vec{B}_{mw}$ is the microwave driving field for $|m_s = 0\rangle$ to $|m_s = \pm 1\rangle$ transition, S_i ($i \in \{x, y, z\}$) are the spin-1 matrices and M_i , N_i ($i \in \{x, y, z\}$) are strain

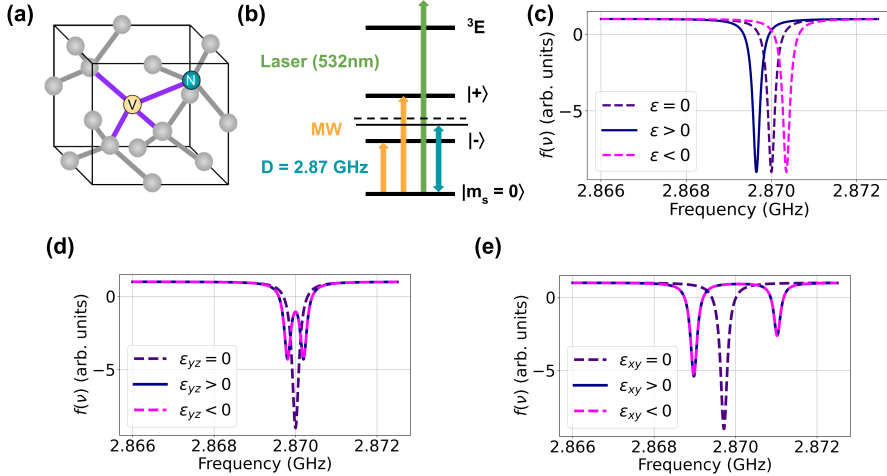


FIGURE 7 (a) Atomic structure of the NV⁻ center in diamond. (b) Electronic structure of the NV⁻ center in the presence of crystal strain. (c) Simulated zero-field ODMR spectra in the presence of volumetric strain. A spectral shift was observed owing to the volumetric strain in the crystal. (d) Simulated zero-field ODMR spectrum in the presence of the pure shear strain. Splitting of the spectrum was observed because of the pure shear strain in the crystal. (e) Simulated zero-field ODMR spectrum in the presence of in-plane shear strain. A spectral shift and asymmetric splitting were observed owing to the in-plane strain in the crystal.

amplitudes [12, 23, 24],

$$M_z = [h_{41}(\epsilon_{xx} + \epsilon_{yy}) + h_{43}\epsilon_{zz}] \quad (6)$$

$$M_x = \frac{1}{2} \left[h_{16}\epsilon_{xz} - \frac{1}{2}h_{15}(\epsilon_{xx} - \epsilon_{yy}) \right] \quad (7)$$

$$M_y = \frac{1}{2} [h_{16}\epsilon_{yz} + h_{15}\epsilon_{xy}] \quad (8)$$

$$N_x = \frac{1}{2} \left[h_{26}\epsilon_{xz} - \frac{1}{2}h_{25}(\epsilon_{xx} - \epsilon_{yy}) \right] \quad (9)$$

$$N_y = \frac{1}{2} [h_{26}\epsilon_{yz} + h_{25}\epsilon_{xy}] \quad (10)$$

The ϵ_{ij} are starting tensor elements in the single NV⁻ center frame, and h_{ij} are the spin-strain coupling parameters [12, 23, 24]. The values of those parameters are shown in Table 2. The values of N_x and N_y are negligible, and these

TABLE 2 Spin-strain coupling strengths [24].

Parameter	Value (GHz)	Parameter	Value (GHz)
h_{43}	2.3 ± 0.2	h_{41}	-6.42 ± 0.09
h_{25}	-2.6 ± 0.08	h_{26}	-2.83 ± 0.07
h_{15}	5.7 ± 0.2	h_{16}	19.66 ± 0.09

terms contribute to the off-diagonal elements of the Hamiltonian [12, 23, 24]. The eigen energies of the ground state Hamiltonian in the absence of the microwave driving field [12, 23, 24],

$$E_{|m_s=0\rangle} = 0, E_{\pm} = \left(D + M_z \pm \sqrt{M_x^2 + M_y^2} \right) \quad (11)$$

Figure 6(a) shows the atomic structure of a single NV center. The electronic energy levels and the corresponding transitions are shown in Figure 6(b). E_{\pm} are the energies of the states $|\pm\rangle$, and the energy gap between the solid and dashed lines is denoted by the strain amplitude M_z . The corresponding eigenstates are,

$$|m_s = 0\rangle = |0\rangle, |\pm\rangle = \frac{1}{\sqrt{2}} \left(\pm e^{i\phi_{str}} | -1 \rangle + | +1 \rangle \right) \quad (12)$$

where $\phi_{str} = \tan^{-1}(M_y/M_x)$ denotes the effective strain vector in-plane angle [23, 24]. From Equation 11, the strain at the position of the NV⁻ center mixes the $|\pm\rangle$ eigenstates [23, 24]. The relevant microwave-driven transitions were $|0\rangle \rightarrow |+\rangle$ and $|0\rangle \rightarrow |-\rangle$. These two transition rates can be determined by solving Equation 12,

$$\alpha_{\pm} = |\langle 0 | \hat{B}_{mw} \cdot \vec{S} | \pm \rangle|^2 \quad (13)$$

$$\Rightarrow \alpha_{\pm} = \frac{1 \pm \cos(2\phi_{mw} + \phi_{str})}{2} \quad (14)$$

where ϕ_{mw} is the angle between $B_{mw,\perp}$ and the NV⁻ center xaxis [23, 24]. Owing to the two superposition states $(|\pm\rangle)$ [23, 24], there are two microwave active transitions in the ODMR spectrum in the absence of a static magnetic field, and the corresponding transition frequencies are $\nu_{\pm} = \frac{1}{\hbar} (D + M_z \pm \sqrt{M_x^2 + M_y^2})$ [23, 24]. Each of these transitions leads to the depletion of the ground-state population, thereby reducing the fluorescence and showing the two dips in the ODMR spectrum. The spectral properties of the NV⁻ center's microwave transitions can be modeled with a Lorentzian profile with a specific line width γ [23, 24],

$$L(\nu) = \frac{\gamma}{\nu^2 + \gamma^2} \quad (15)$$

and the spectrum of a single NV⁻ center in the presence of crystal strain is

$$f(\nu) = 1 - A[\alpha_+ L(\nu - \nu_+) + \alpha_- L(\nu - \nu_-)]$$

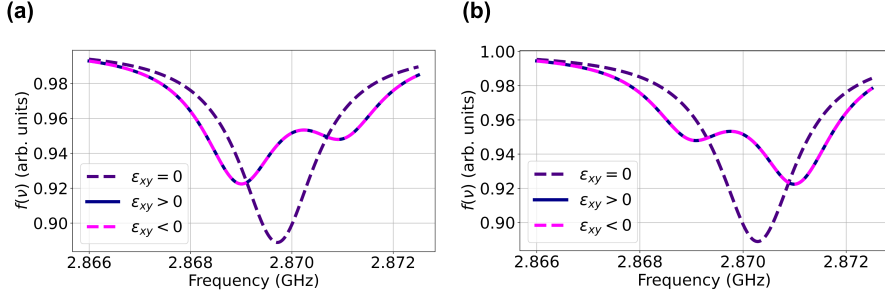


FIGURE 8 (a) Simulated zero-field ODMR spectrum of the NV^- center in an ion-implanted bulk diamond sample. (b) Simulated zero-field ODMR spectrum of the NV^- center in the diamond nanopillar sample.

$$\Rightarrow f(v) = 1 - A \left[\left(\frac{1 + \cos(2\phi_{mw} + \phi_{str})}{2} \right) \left(\frac{\gamma}{(v - v_+)^2 + \gamma^2} \right) + \left(\frac{1 - \cos(2\phi_{mw} + \phi_{str})}{2} \right) \left(\frac{\gamma}{(v - v_-)^2 + \gamma^2} \right) \right]$$

$$\begin{aligned} \Rightarrow f(v) = 1 - A \left(\frac{1 + \cos(2\phi_{mw} + \phi_{str})}{2} \right) & \left(\frac{\gamma}{\left(v - \left(\frac{1}{\hbar} \left(D + M_z + \sqrt{(M_x^2 + M_y^2)} \right) \right) \right)^2 + \gamma^2} \right) - \\ A \left(\frac{1 - \cos(2\phi_{mw} + \phi_{str})}{2} \right) & \left(\frac{\gamma}{\left(v - \left(\frac{1}{\hbar} \left(D + M_z - \sqrt{(M_x^2 + M_y^2)} \right) \right) \right)^2 + \gamma^2} \right). \end{aligned} \quad (16)$$

Strain can affect the zero-field ODMR spectral profile based on the presence of strain tensor components. For volumetric strain $\epsilon = (\epsilon_{xx} + \epsilon_{yy} + \epsilon_{zz})$ [23, 24], a spectral shift was observed in the zero-field ODMR simulation. The compressive strain or negative value of ϵ shifts the zero-field ODMR spectra towards the higher frequency regime, whereas the tensile strain or positive value of ϵ shifts the spectrum towards the lower frequency regime. Figure 7(c) shows the effect of the compressive and tensile strain on the zero-field ODMR spectrum [23, 24]. Owing to the presence of shear strain in the YZ plane, the $|+1\rangle$ and $| -1\rangle$ spin states form superposition states $|\pm\rangle$. The energy difference between the two superposition states develops a symmetric splitting in the zero-field ODMR spectrum [12, 23, 24]. Figure 7(d) shows the simulated zero-field ODMR spectrum in the presence of the shear strain in the YZ plane. There is another kind of shear strain in the XY-plane, where ϵ_{xx} , ϵ_{yy} , and ϵ_{xy} are non-zero and $\epsilon_{zz} = 0$ [23, 24]. In this type of scenario, there is a spectral shift as well as an imbalance or asymmetric splitting in the zero-field ODMR

data. Figure 7(e) shows the simulated zero-field ODMR spectrum for different regimes of ϵ_{xy} [23, 24]. The spectral shift ($\Delta\nu$), splitting ($\delta\nu$) of the $|\pm\rangle$ states, and spectral imbalance (I) can be quantified using Equations 17, 18, and 19, respectively.

$$\Delta\nu = \frac{(\nu_+ + \nu_-)}{2} - D = M_z \quad (17)$$

$$\delta\nu = (\nu_+ - \nu_-) = 2\sqrt{M_x^2 + M_y^2} \quad (18)$$

$$I = \frac{\alpha_+ - \alpha_-}{\alpha_+ + \alpha_-}. \quad (19)$$

Asymmetric splitting was observed owing to shear strain for both the N-ion-implanted diamond sample and the diamond nanopillar sample. However, no spectral shift was observed in the zero-field ODMR spectrum. Figure 5(d) and 6(b) show the experimentally observed zero-field ODMR spectra for the nitrogen ion-implanted sample and diamond nanopillar sample, respectively. Similarly, figure 8 (a) and (b) show the simulated ODMR spectra of both samples. The only distinction between the two scenarios was the value of ϕ_{mw} ; otherwise, the strain parameters were identical. The ion-implanted and diamond nanopillar samples had 0 and $\pi/2$ for ϕ_{mw} , respectively.

3 | CONCLUSION

In conclusion, we report the observation of asymmetric splitting in the zero-field CW-ODMR spectrum of both nitrogen ion-implanted and diamond nanopillar samples due to the shear strain in the XY plane. We employ a measurement methodology to characterize the crystal strain affecting the NV^- center's electronic spin. To explain and quantify the observed asymmetry, we demonstrate a model that attributes the effect to strain in the diamond lattice.

Efficient light-matter interaction is essential for quantum communication applications, particularly for transferring quantum information to spin qubits or generating entanglement between distant qubits via single-photon detection schemes [1]. Similarly, high photon collection efficiency is critical for both quantum information processing and quantum sensing, as it directly influences overall system performance [1]. Ion implantation and the nanofabrication of diamond photonic structures are, therefore, key technologies for enabling and enhancing these capabilities. Ion implantation followed by subsequent annealing results in the formation of NV centers within the diamond matrix, accompanied by minimal lattice disorder at lower doses. Increasing ion doses lead to significant lattice distortion, resulting in splitting and asymmetry in the ODMR spectra.

Zero-field ODMR provides a powerful tool for characterizing strain components in diamond crystals, yielding insights into qubit coherence, performance, and calibration of quantum gates [42] as well as the optical properties of emitted photons [38]. This approach offers a valuable framework for assessing and optimizing device performance across quantum information, sensing, and communication platforms.

4 | EXPERIMENTAL DETAILS

The ion-implanted samples were characterized using a confocal Micro-Raman spectrometer (Horiba Jobin Yvon LAB RAM HR Evolution) in backscattering geometry (resolution 0.1 cm^{-1}), employing a 532 nm diode laser as the excitation

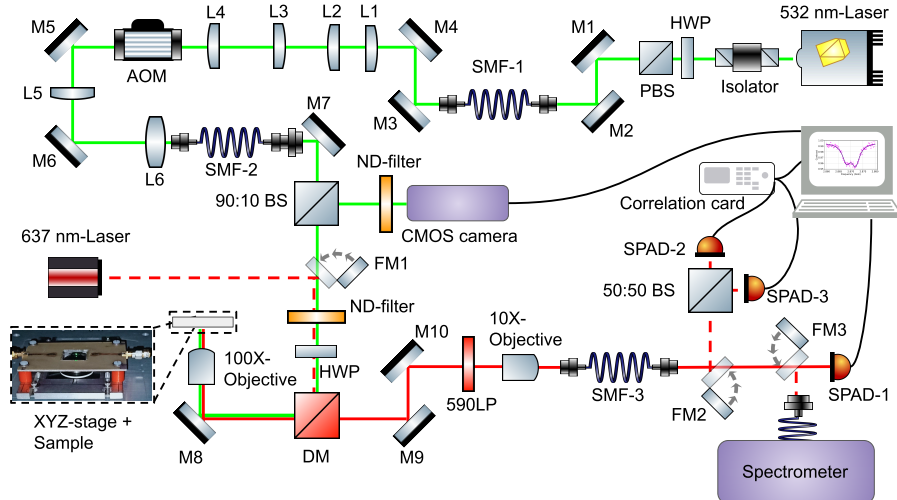


FIGURE 9 Schematic diagram of the home-built laser scanning confocal microscope with microwave excitation setup. Abbreviation-L: Plano convex lens, M: Broadband dichroic mirrors, HWP: Half wave plate, PBS: Polarizing beam splitter, SMF: Single-mode fiber, AOM: Acousto-optic modulator, ND-filter: Neutral density filters, DM: Dichroic mirror, LP: Long-pass filter, FM: Flip mirror, BS: Beam splitter, SPAD: Single-photon avalanche diode.

source. For quantitative impurity analysis, optical absorbance spectra were recorded using a UV-Visible spectrophotometer (Carry 100-UV-Vis from Agilent).

A laser-scanning confocal microscope with microwave excitation was used for strain measurement in the diamond samples. A continuous-wave (CW) 532 nm diode-pumped solid-state (DPSS) laser (Sprout-G-5W from Lighthouse Photonics) was used for the optical pumping. A half-wave plate (HWP) and polarizing beam splitter (PBS) combination controls the laser power. An acoustic-optic modulator (M1133-aQ80L-1 from Isomet) was added to the excitation path to pulse the 532 nm laser. A single-mode fiber (P3-405B-FC-1 from Thorlabs) was used for spatial filtering to create a clean Gaussian 532 nm excitation beam. The collimated, clean Gaussian was sent to the 90:10 beam splitter (BS), followed by a dichroic mirror (532 nm laser BrightLine dichroic beam splitter from Semrock) to separate the excitation beam and the NV-center emission spectra. A 590 nm long-pass filter (ET590lp from Chroma) was used for spectral filtering and to achieve a better signal-to-noise ratio. A 10X objective lens is used to focus down the beam in the detection path, and a single-mode fiber is placed at the focal spot of the objective lens, which acts as a pinhole system for detecting light from the focal spot of the 100X objective lens inside the diamond crystal sample. In the detection path, a single-photon avalanche diode (SPCM-AQRH-4X from Excelitas) was used for imaging and PL collection for ODMR measurement. A flip mirror couples the Hanbury Brown and Twiss (HBT) setup for second-order correlation measurements (correlation card Time Tagger Ultra from Swabian Instruments) or anti-bunching measurements. A three-axis piezo nanopositioning stage (Nano-LP200, Mad City Labs Inc.) was used to scan the diamond crystal and diamond nanopillar sample. Figure 9 shows a schematic of the laser scanning confocal microscope with the microwave excitation setup.

Acknowledgements

K. Saha acknowledges financial support from the National Quantum Mission (NQM) and the Chanakya Doctoral Fellowship for A. Majumder and A. Bathla. Authors also acknowledge the IIT Bombay Nanofabrication Facility (Centre of Excellence in Nanoelectronics) and the Sophisticated Analytical Instrument Facility (SAIF)/ Center for Research in Nano Technology and Science (CRNTS), IIT Bombay, for support in diamond nanopillar fabrication and optical characterization, respectively. Authors also acknowledge the insightful contributions of Dr. Bikash D. Choudhury for the initial fabrication of diamond nanopillars. P. Rai acknowledges the funding support from the SERB (CRG/2021/000696) and DAE (DPR-6/3(1)/2018/UM-DAE-CBS/R&D-II/8971). The authors acknowledge the Solid State Physics Laboratory (SSPL), New Delhi, India, for the ion implantation facility. The authors would like to thank Alexander Franzen for creating the illustration of the optical components.

Author contributions

AM performed the ODMR experiments and NV ODMR simulations. VKS conducted the SRIM simulations and Raman spectroscopy measurements. AB fabricated the diamond nanopillars, while BSY and NS carried out the ion implantation. AM and VKS prepared the manuscript in consultation with KS and PR, who supervised all aspects of the work.

Conflict of interest

The authors declare no conflict of interest.

Supporting Information

For a single NV⁻ center oriented along the lab frame's polar and azimuth angles θ and ϕ , respectively, with a symmetry axis [31, 43]

$$\hat{e}_{NV} = \begin{pmatrix} \sin \theta \cos \phi \\ \sin \theta \sin \phi \\ \cos \theta \end{pmatrix} \quad (20)$$

Its two mutually orthogonal dipoles \vec{d}_1 and \vec{d}_2 with dipole moment d are,

$$\vec{d}_1 = d \begin{pmatrix} -\sin \phi \\ \cos \phi \\ 0 \end{pmatrix}, \vec{d}_2 = d \begin{pmatrix} \cos \theta \cos \phi \\ \cos \theta \sin \phi \\ -\sin \theta \end{pmatrix} \quad (21)$$

For our case, the surface orientation of the diamond sample is [100], and the corresponding four possible NV⁻ orientations and the associated dipole orientations are listed in Table 3.

TABLE 3 NV-axis and dipole vector orientations with corresponding spherical angles.

NV Orientation	Vector	Cartesian Components	Spherical Angles (°)
NV-1	\vec{e}_{NV}	[-0.229, -0.805, -0.547]	$\theta = 123.14, \phi = 254.14$
	\vec{d}_1	[-0.962, 0.273, 0.0]	$\theta = 90.00, \phi = 164.14$
	\vec{d}_2	[0.149, 0.526, -0.837]	$\theta = 146.86, \phi = 74.14$
NV-2	\vec{e}_{NV}	[-0.773, 0.239, 0.588]	$\theta = 53.98, \phi = 162.81$
	\vec{d}_1	[0.296, 0.955, -0.0]	$\theta = 90.00, \phi = 72.81$
	\vec{d}_2	[-0.562, 0.174, -0.809]	$\theta = 143.98, \phi = 162.81$
NV-3	\vec{e}_{NV}	[0.238, 0.766, -0.597]	$\theta = 126.64, \phi = 72.75$
	\vec{d}_1	[0.955, -0.297, 0.0]	$\theta = 90.00, \phi = 342.75$
	\vec{d}_2	[-0.177, -0.57, -0.802]	$\theta = 143.36, \phi = 252.75$
NV-4	\vec{e}_{NV}	[0.813, -0.236, 0.533]	$\theta = 57.80, \phi = 343.79$
	\vec{d}_1	[-0.279, -0.96, 0.0]	$\theta = 90.00, \phi = 253.79$
	\vec{d}_2	[0.512, -0.149, -0.846]	$\theta = 147.8, \phi = 343.79$

References

- [1] Ruf M, Wan NH, Choi H, Englund D, Hanson R. Quantum networks based on color centers in diamond. *Journal of Applied Physics* 2021;130(7).
- [2] Suter D, Jelezko F. Single-spin magnetic resonance in the nitrogen-vacancy center of diamond. *Progress in nuclear magnetic resonance spectroscopy* 2017;98:50–62.
- [3] Wolfowicz G, Heremans FJ, Anderson CP, Kanai S, Seo H, Gali A, et al. Quantum guidelines for solid-state spin defects. *Nature Reviews Materials* 2021;6(10):906–925.
- [4] Du J, Shi F, Kong X, Jelezko F, Wrachtrup J. Single-molecule scale magnetic resonance spectroscopy using quantum diamond sensors. *Reviews of Modern Physics* 2024;96(2):025001.
- [5] Bucher DB, Aude Craik DP, Backlund MP, Turner MJ, Ben Dor O, Glenn DR, et al. Quantum diamond spectrometer for nanoscale NMR and ESR spectroscopy. *Nature protocols* 2019;14(9):2707–2747.
- [6] Pezzagna S, Meijer J. Quantum computer based on color centers in diamond. *Applied Physics Reviews* 2021;8(1).
- [7] Levine EV, Turner MJ, Kehayias P, Hart CA, Langellier N, Trubko R, et al. Principles and techniques of the quantum diamond microscope. *Nanophotonics* 2019;8(11):1945–1973.
- [8] Rondin L, Tetienne JP, Hingant T, Roch JF, Maletinsky P, Jacques V. Magnetometry with nitrogen-vacancy defects in diamond. *Reports on progress in physics* 2014;77(5):056503.
- [9] Modak A, Majumder A, Parashar M, Tallur S, Saha K. Few NV Center Nanodiamonds Enable High-Speed and High-Resolution Sensing of Paramagnetic Species. In: 2023 Joint Conference of the European Frequency and Time Forum and IEEE International Frequency Control Symposium (EFTF/IFCS) IEEE; 2023. p. 1–3.

[10] Mzyk A, Sigaeva A, Schirhagl R. Relaxometry with nitrogen vacancy (NV) centers in diamond. *Accounts of Chemical Research* 2022;55(24):3572–3580.

[11] Parashar M, Bathla A, Shishir D, Gokhale A, Bandyopadhyay S, Saha K. Sub-second temporal magnetic field microscopy using quantum defects in diamond. *Scientific reports* 2022;12(1):8743.

[12] Barry JF, Schloss JM, Bauch E, Turner MJ, Hart CA, Pham LM, et al. Sensitivity optimization for NV-diamond magnetometry. *Reviews of Modern Physics* 2020;92(1):015004.

[13] Janitz E, Bhaskar MK, Childress L. Cavity quantum electrodynamics with color centers in diamond. *Optica* 2020;7(10):1232–1252.

[14] Majumder A, Choudhury BD, Saha K. Engineering a mechanically stable hybrid photonic crystal cavity coupled to color defects in diamond. *Journal of Optics* 2022;24(6):064014.

[15] Knaut CM, Suleymanzade A, Wei YC, Assumpcao DR, Stas PJ, Huan YQ, et al. Entanglement of nanophotonic quantum memory nodes in a telecom network. *Nature* 2024;629(8012):573–578.

[16] Reiserer A, Rempe G. Cavity-based quantum networks with single atoms and optical photons. *Reviews of Modern Physics* 2015;87(4):1379–1418.

[17] Baier S, Bradley C, Middelburg T, Dobrovitski V, Taminiau T, Hanson R. Orbital and spin dynamics of single neutrally-charged nitrogen-vacancy centers in diamond. *Physical Review Letters* 2020;125(19):193601.

[18] Pfaff W, Taminiau TH, Robledo L, Bernien H, Markham M, Twitchen DJ, et al. Demonstration of entanglement-by-measurement of solid-state qubits. *Nature Physics* 2013;9(1):29–33.

[19] Harris IB, Christen I, Patomäki SM, Raniwala H, Sirotin M, Colangelo M, et al. High-Fidelity Control of a Strongly Coupled Electro-Nuclear Spin-Photon Interface. *arXiv preprint arXiv:250509267* 2025;.

[20] Marseglia L, Saha K, Ajoy A, Schröder T, Englund D, Jelezko F, et al. Bright nanowire single photon source based on SiV centers in diamond. *Optics express* 2018;26(1):80–89.

[21] McCloskey DJ, Dontschuk N, Broadway DA, Nadarajah A, Stacey A, Tetienne JP, et al. Enhanced widefield quantum sensing with nitrogen-vacancy ensembles using diamond nanopillar arrays. *ACS applied materials & interfaces* 2020;12(11):13421–13427.

[22] Liang W, Yang L, Zhu J, Lian Y, Lu Y. Strain engineering of microfabricated diamond and its applications. *APL Materials* 2025;13(6).

[23] Alam MS, Gorrini F, Gawełczyk M, Wigger D, Coccia G, Guo Y, et al. Determining strain components in a diamond waveguide from zero-field optically detected magnetic resonance spectra of negatively charged nitrogen-vacancy-center ensembles. *Physical Review Applied* 2024;22(2):024055.

[24] Udvarhelyi P, Shkolnikov VO, Gali A, Burkard G, Pályi A. Spin-strain interaction in nitrogen-vacancy centers in diamond. *Physical Review B* 2018;98(7):075201.

[25] Bates KM, Day MW, Smallwood CL, Owen RC, Schröder T, Bielejec E, et al. Using silicon-vacancy centers in diamond to probe the full strain tensor. *Journal of Applied Physics* 2021;130(2).

[26] Klotz M, Tangemann A, Kubanek A. Ultra-high strained diamond spin register with coherent optical control. *npj Quantum Information* 2025;11(1):1–8.

[27] Grazioso F, Patton BR, Delaney P, Markham ML, Twitchen DJ, Smith JM. Measurement of the full stress tensor in a crystal using photoluminescence from point defects: The example of nitrogen vacancy centers in diamond. *Applied Physics Letters* 2013;103(10).

- [28] Trusheim ME, Englund D. Wide-field strain imaging with preferentially aligned nitrogen-vacancy centers in polycrystalline diamond. *New Journal of Physics* 2016;18(12):123023.
- [29] Shukla VK, Majumder A, Yadav BS, Dalal S, Singh N, Saha K, et al. Anti-bunching behavior of photons and strain determination in boron-implanted single-crystal diamond using irradiation induced nitrogen-vacancies. *Diamond and Related Materials* 2025;p. 112388.
- [30] Ziegler JF, Biersack JP. SRIM-2008, stopping power and range of ions in matter. International Atomic Energy Agency 2008;.
- [31] Reuschel P, Agio M, Flatae AM. Vector magnetometry based on polarimetric optically detected magnetic resonance. *Advanced Quantum Technologies* 2022;5(11):2200077.
- [32] Uzan-Saguy C, Cytermann C, Brener R, Richter V, Shaanan M, Kalish R. Damage threshold for ion-beam induced graphitization of diamond. *Applied Physics Letters* 1995;67(9):1194–1196.
- [33] Jiménez-Riobóo R, Gordillo N, de Andrés A, Redondo-Cubero A, Moratalla M, Ramos M, et al. Boron-doped diamond by 9 MeV microbeam implantation: Damage and recovery. *Carbon* 2023;208:421–431.
- [34] Shukla VK, Lekshmi J, Yadav BS, Kumari M, Dalal S, Goyal A, et al. The influence of nitrogen and boron doping on the surface morphology, defects and crystallinity of large-area chemical vapor deposition grown single crystal diamond. *International Journal of Refractory Metals and Hard Materials* 2024;119:106559.
- [35] Nistor S, Stefan M, Ralchenko V, Khomich A, Schoemaker D. Nitrogen and hydrogen in thick diamond films grown by microwave plasma enhanced chemical vapor deposition at variable H 2 flow rates. *Journal of Applied Physics* 2000;87(12):8741–8746.
- [36] Mouradian S, Wan NH, Schröder T, Englund D. Rectangular photonic crystal nanobeam cavities in bulk diamond. *Applied Physics Letters* 2017;111(2).
- [37] Doherty MW, Manson NB, Delaney P, Jelezko F, Wrachtrup J, Hollenberg LC. The nitrogen-vacancy colour centre in diamond. *Physics Reports* 2013;528(1):1–45.
- [38] Maze JR, Gali A, Togan E, Chu Y, Trifonov A, Kaxiras E, et al. Properties of nitrogen-vacancy centers in diamond: the group theoretic approach. *New Journal of Physics* 2011;13(2):025025.
- [39] Fávaro de Oliveira F, Momenzadeh SA, Antonov D, Scharpf J, Osterkamp C, Naydenov B, et al. Toward optimized surface δ -profiles of nitrogen-vacancy centers activated by helium irradiation in diamond. *Nano letters* 2016;16(4):2228–2233.
- [40] Lobaev M, Gorbachev A, Bogdanov S, Vikharev A, Radishev D, Isaev V, et al. Influence of CVD diamond growth conditions on nitrogen incorporation. *Diamond and Related Materials* 2017;72:1–6.
- [41] Balmer R, Brandon J, Clewes S, Dhillon H, Dodson J, Friel I, et al. Chemical vapour deposition synthetic diamond: materials, technology and applications. *Journal of Physics: Condensed Matter* 2009;21(36):364221.
- [42] Bartling HP, Yun J, Schymik KN, van Riggelen M, Enthoven LA, van Ommeren HB, et al. Universal high-fidelity quantum gates for spin qubits in diamond. *Phys Rev Appl* 2025 Mar;23:034052. <https://link.aps.org/doi/10.1103/PhysRevApplied.23.034052>.
- [43] Zhu Y, Wang Y, Fang D, Wu H, Zhou H, Yu Z, et al. Visualized Axial Localization of Nitrogen-Vacancy Center in Bulk Diamond Assisted by Radially Polarized Beam. *ACS Photonics* 2024;11(10):4357–4364.